

A Unified Platform and Quality Assurance Framework for 3D Ultrasound Reconstruction with Robotic, Optical, and Electromagnetic Tracking

Lewis Howell^{1,2}, Manisha Waterston^{1,2}, Tze Min Wah^{3,4}, James H. Chandler², and James R. McLaughlan^{2,4}

¹School of Computer Science, University of Leeds, Leeds, LS2 9JT

²School of Electronic and Electrical Engineering, University of Leeds, Leeds, LS2 9JT

³St James's University Hospital, Leeds Teaching Hospitals NHS Trust, LS9 7TF

⁴Leeds Institute of Medical Research, University of Leeds, St James' University Hospital, Leeds, LS9 7TF

March 23, 2026

Abstract

Three-dimensional (3D) Ultrasound (US) can facilitate diagnosis, treatment planning, and image-guided therapy. However, current studies rarely provide a comprehensive evaluation of volumetric accuracy and reproducibility, highlighting the need for robust Quality Assurance (QA) frameworks, particularly for tracked 3D US reconstruction using freehand or robotic acquisition.

This study presents a QA framework for 3D US reconstruction and a flexible open source platform for tracked US research. A custom phantom containing geometric inclusions with varying symmetry properties enables straightforward evaluation of optical, electromagnetic, and robotic kinematic tracking for 3D US at different scanning speeds and insonation angles.

A standardised pipeline performs real-time segmentation and 3D reconstruction of geometric targets (DSC = 0.97, FPS = 46) without GPU acceleration, followed by automated registration and comparison with ground-truth geometries. Applying this framework showed that our robotic 3D US achieves state-of-the-art reconstruction performance (DSC-3D = 0.94 ± 0.01 , HD95 = 1.17 ± 0.12), approaching the spatial resolution limit imposed by the transducer.

This work establishes a flexible experimental platform and a reproducible validation methodology for 3D US reconstruction. The proposed framework enables robust cross-platform comparisons and improved reporting practices, supporting the safe and effective clinical translation of 3D ultrasound in diagnostic and image-guided therapy applications.

Keywords: Ultrasound, 3D reconstruction, Quality assurance, Robotic ultrasound, Imaging guidance.

1 Introduction

Ultrasound (US) is widely used to image soft tissues, providing a non-ionising, low-cost, portable, and real-time imaging modality [1]. Beyond diagnostic applications, US also supports intra-operative guidance [2], image-guided biopsy [3], microwave and radiofrequency ablation [4, 5], and emerging non-invasive modalities such as High-Intensity Focused Ultrasound (HIFU) and histotripsy [6, 7, 8]. In these applications, spatial understanding of the relative shapes and positions of anatomical structures is critical to ensure diagnostic accuracy, safety, and treatment efficacy. However, traditional Two-dimensional (2D) US provides a limited cross-sectional field of view, which reduces options for volumetric analysis and makes US-guided applications dependent on the operator’s scanning technique and skill in geometric reasoning [9, 10].

Tracked Three-dimensional (3D) US addresses this limitation by combining conventional 2D imaging with position and orientation tracking to reconstruct 3D anatomy [11, 12]. Compared with dedicated 3D transducers, this approach enables reconstruction over larger areas, uses widely available and more cost-effective 2D transducers and machines, and can be readily integrated with imaging-guidance systems [13, 11, 14]. To acquire position and orientation tracking data, optical and electromagnetic (EM) tracking have been used in freehand approaches [12]. For example, Chung *et al.* demonstrated freehand optical-tracked US for carotid artery 3D imaging [14], while Krönke *et al.* applied EM-tracked US for thyroid volumetry, demonstrating improved repeatability relative to standard 2D approaches [15]. More recently, robotic US has improved scanning stability, trajectory control, and pose estimation [16]. Faoro *et al.* used robotic US for 3D vessel reconstruction as a pre-treatment planning step for transcarotid revascularisation [17], Sun *et al.* demonstrated 3D musculoskeletal imaging [18], and Zhou *et al.* proposed a robotic US system for kidney and lesion imaging for HIFU imaging-guidance. Robotic kinematic tracking can be used independently for pose estimation or combined with optical or EM tracking to simplify co-registration with patient or tool coordinate frames, supporting multimodal image guidance and interventional workflows [19].

Despite widespread investigation of tracked US for 3D reconstruction, there is currently no standardised Quality Assurance (QA) framework specifically designed to validate tracked 3D US reconstruction systems. Existing commercial QA phantoms are expensive and intended primarily to assess 2D or dedicated 3D transducers [13]. Consequently, most existing tracked US studies report task-specific outcomes, such as 3D measurement accuracy for a specific organ, but lack a comprehensive evaluation of their systems’ capabilities. Task-specific metrics are often also dependent on segmentation of the test object, meaning that errors associated with calibration, tracking, and 3D reconstruction cannot be isolated from those of anatomical segmentation models (often black-box Artificial Intelligence (AI)-based) used to process the US images. The robustness of these systems is also rarely assessed, particularly how scanning speed and insonation angle affect the quality and reliability of 3D reconstruction. This makes cross-system comparisons difficult, thereby limiting evidence-based development.

To address this, we present two complementary contributions. First, we introduce a flexible, open source tracked US platform for 3D reconstruction that supports interchangeable pose estimation using kinematic, optical, or EM tracking within a unified coordinate system. Second, we present an open source QA framework for evaluating tracked 3D US reconstruction, including a purpose-designed agar phantom with geometric inclusions (sphere, ellipsoid, cylinder, and triangular prism) to enable direct comparison with ground-truth volumes. Using controlled scanning and simultaneous multimodal tracking, we compare kinematic, optical, and EM tracking for 3D reconstruction, providing insights for future research.

2 Methods

This study presents a flexible platform for 3D US that integrates conventional brightness-mode (B-mode) US imaging with robotic, optical, or EM tracking. The workflow for 3D reconstruction comprised four stages: (A) tracked image acquisition, (B) calibration and spatial registration, (C) segmentation and 3D

reconstruction, (D) quality assurance.

2.1 Tracked Image Acquisition

The system uses open source tools to support integration with multiple imaging and tracking systems. Modules for data acquisition, robotic navigation, data streaming, segmentation, and visualisation ran on a distributed system using OpenIGTLink for real-time communication [20] (Fig. 1). ROS2 (Foxy) interfaced with the robot and optical tracking systems, PLUS (v2.9.0) handled coordination synchronisation [21], and 3DSlicer (v5.2.2) with SlicerIGT enabled visualisation, reconstruction, and analysis [22]. Segmentation and 3D reconstruction were implemented in Python 3.9 on an Ubuntu 20.04 workstation (Intel i7, 32 GB RAM). Full instructions for the system setup, as well as relevant scripts, configuration files, and example code is included in the GitHub repository (<https://github.com/SMRTUS/US-QA-3D>).

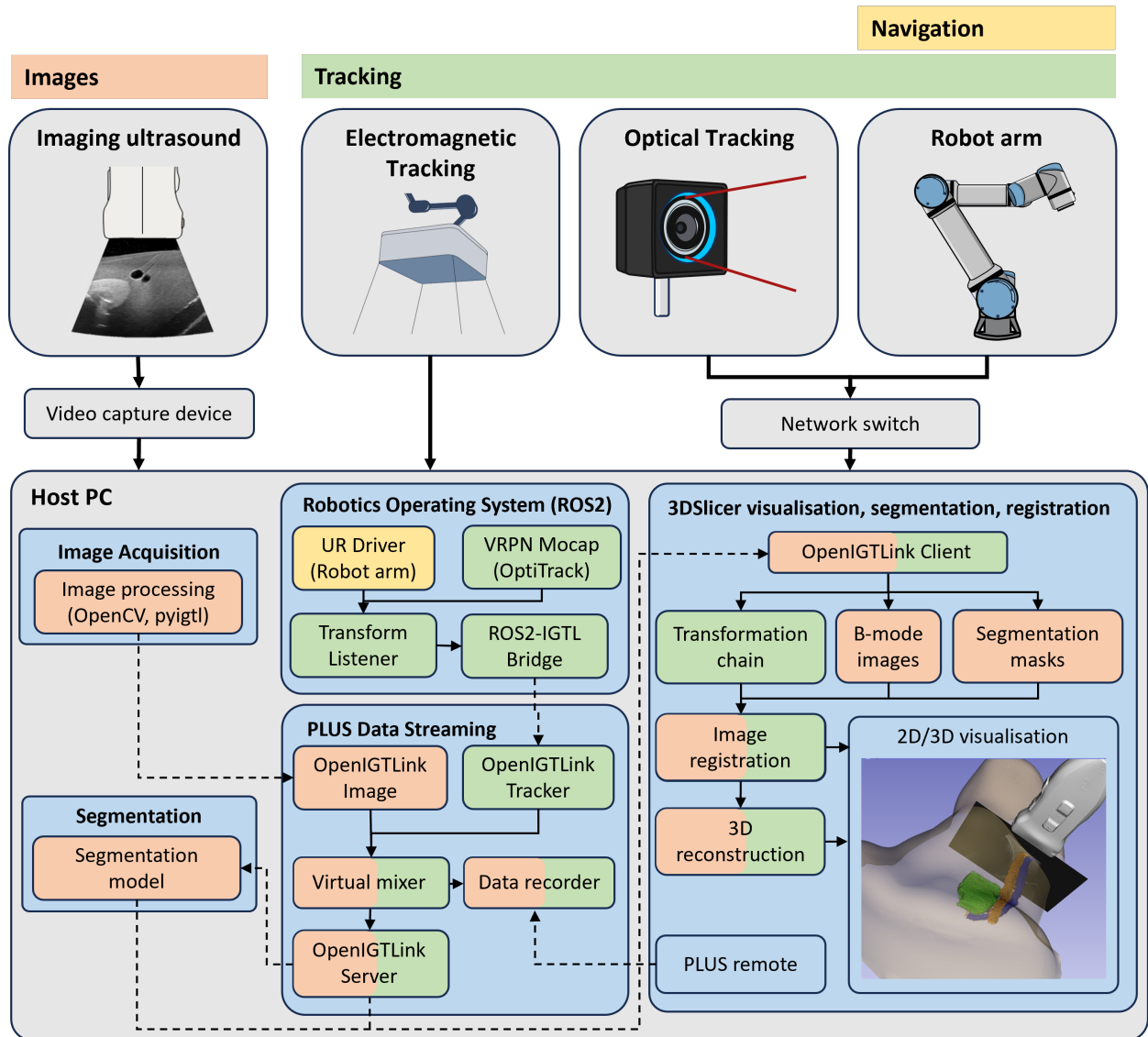


Figure 1: Technical diagram showing hardware devices (grey) and software modules (blue) included as part of the experimental system used for real-time 3D US reconstruction. The OpenIGTLink protocol was used to exchange data between modules (dashed arrows). The data flow within modules (thin solid arrows) and connections between hardware devices are also shown (thick solid arrows).

US images were acquired using a point-of-care US system (GE, Venue Fit) and a L4-20t-RS transducer (3–20 MHz, 38.4 mm field of view (FOV)) and frames were captured with an HDMI-to-USB 3.0 capture

card (Magewell, USB Capture HDMI Gen 2) and processed at the scanner’s native resolution (1920x1080) and frame rate (15-30 FPS) using OpenCV. This acquisition approach is broadly compatible with modern US systems providing HDMI output, though device-specific APIs may reduce latency.

High-resolution harmonic B-mode imaging used 10/20 MHz frequency, 78 dB dynamic range, speckle reduction, and virtual convex mode to extend the FOV. Using these imaging parameters, the axial, lateral, and elevational resolution (slice thickness) were 0.25-0.5 mm, 0.5-1.0 mm, and 0.7-2.0 mm respectively at 3 cm focal depth, measured using a multipurpose QA phantom (CIRS, 040GSE) [23].

A 6 Degrees of Freedom (DoF) collaborative robotic arm (Universal Robots, UR3e) was used to move and track the transducer pose. The transducer was secured in a custom two-part 3D-printed holder mounted onto the robot flange. The robot was interfaced via ROS2 and the Universal Robots drivers [24], which provided real-time pose estimates based on the robot’s internal kinematics. A custom ROS2 transform listener converted axis-angle-representation poses to transformation matrices and streamed them to PLUS via the ROS2-IGTL-bridge [25]. The module MoveIt for ROS2 was used for motion planning [26] to generate consistent scanning trajectories. Baseline QA scans used linear translation at 5.0 mm/s, unless otherwise stated.

The transducer’s position and orientation were also captured using optical and EM tracking. The optical tracking system used four infrared cameras (OptiTrack, Prime 13), positioned to maximise coverage of the working area, and calibrated using a standard wand-based dynamic calibration (OptiTrack Motive v2.2.0) [27]. A rigid-body frame with four 6.4 mm retroreflective markers was mounted to the transducer holder for passive tracking. A ROS2 VRPN client [28] broadcast timestamped poses at 60 FPS, and a custom ROS2 listener forwarded the timestamped transformations to PLUS via ROS2-IGTL-bridge [29].

EM tracking used a Planar 20-20 Field Generator, control unit, sensor interface unit, and 6-DoF sensor (NDI, Aurora), with manufacturer-reported positioning accuracy of 0.48 mm and orientation accuracy of 0.3° [30]. The field generator covered a 500 mm^3 workspace and was positioned to minimise electromagnetic interference (EMI). The control unit was connected via USB 3.1, and timestamped poses were acquired directly through PLUS’s native Aurora interface (Fig. 1) [31].

2.2 Calibration and registration

Static transforms defining the system geometry included the flange-to-transducer offset from Computer-Aided Design (CAD) measurements, robot linkage transforms from Denavit-Hartenberg (DH) parameters [32], image-to-transducer transform from spatial calibration, and coordinate registration transforms. These were organised in 3DSlicer using the Medical Reality Modelling Language (MRML) transform hierarchy, enabling consistent propagation of dynamic motion and tracing of US image coordinates relative to the robot base.

Temporal and spatial calibration were performed using the PLUS freehand calibration tool (fCal) [21]. Temporal calibration estimated the latency between the image and tracking streams by imaging the bottom of a water tank while moving the transducer in a periodic oscillatory motion. Spatial calibration determined the static transform between the US image and the transducer (ImageToTransducer) using a 3-layer N-wire phantom [33], giving a sub-millimetre registration error.

All tracking modalities (robotic, optical, and EM) were aligned to a common world coordinate system defined by the robot base frame. Rigid transforms between coordinate-tracking systems were computed via fiducial registration using at least 8 reference points across the workspace. The 3DSlicer volume reslice driver rendered the US image within the 3D scene during scanning.

2.3 Segmentation and 3D reconstruction

Real-time 3D reconstruction combined frame-by-frame segmentation with voxel-based volume mapping, providing live visual feedback. Segmentation ran in parallel with the imaging pipeline, so the latency from

model inference did not bottleneck visualisation. Tracked frames were processed to produce segmentation masks which retained the original pose and timestamp for synchronised 3D reconstruction.

A threshold-based model segmented anechoic targets in B-mode images of the phantom for QA (D). Processing steps included Region of Interest (ROI) cropping, median filtering (kernel size 7) to reduce speckle noise while preserving edges, and Otsu’s thresholding to create binary masks [34, 35]. Masks were refined using morphological closing to fill gaps and morphological opening to remove small islands. A trimming function removed dark vertical regions from poor coupling. The resulting binary masks were then used as the input for 3D reconstruction.

Real-time 3D reconstruction used the PLUS Volume Reconstruction module in 3DSlicer (SlicerIGT) [22], with voxel-based forward mapping to transform each 2D pixel into a 3D voxel coordinate, and nearest neighbour interpolation to assign voxel values within a pre-defined grid [11]. When multiple pixels mapped to the same voxel, the final value was determined by maximum-value compounding.

Volumes were updated continuously and rendered using 3DSlicer’s Visualisation Toolkit (VTK) GPU Ray Casting, enabling real-time 2D and 3D visualisation [36]. Segmentation overlays were displayed on synchronised B-mode images, and multiplanar formatting allowed for axial, sagittal, coronal, or oblique views of the resulting volumes. This allowed for clear visualisation of anatomical details, aligned with patient anatomy or procedural targets, regardless of the original scan orientation [11].

2.4 Evaluation and Quality Assurance

To evaluate reconstruction accuracy and repeatability, a purpose-built phantom for Ultrasound Quality Assurance in 3-Dimensions (US-QA-3D) was developed. The phantom contained four inclusions with known geometry: a sphere, an ellipsoid, a cylinder, and an equilateral triangular prism, selected for their varied geometric properties and relevance to anatomical structures. The inclusions were cast from an agar mixture without acoustic scatterers, producing anechoic targets whose dimensions serve as ground truth for 3D reconstruction. Inclusions were embedded in a tissue-mimicking agar block containing polydisperse glass beads to introduce speckle noise on B-mode, creating clear contrast against the anechoic targets. Phantom preparation details are provided in Appendix 6.1.

QA experiments were conducted with the phantom suspended in a large water tank filled with filtered, degassed water. This ensured consistent acoustic coupling and unrestricted robot motion. The phantom was scanned using robotic navigation with simultaneous EM, optical, and robotic kinematic tracking (Fig. 2.4). Optical cameras were arranged to maximise marker visibility, and the EM field generator was positioned to minimise EMI, without restricting probe motion. A ~ 1 cm water layer separated the transducer from the phantom to prevent target deformation.

Baseline scans used automated linear trajectories at 5.0 mm/s, with the imaging plane orthogonal to the phantom’s long axis. Additional experiments varied scan speed (2.5–17.5 mm/s) and insonation angles (30° , 45° , and 90° about the axial axis and $\pm 20^\circ$ about the lateral axis). At large axial angles, multi-sweep scans were required due to the limited B-mode FOV, and overlapping regions were combined using maximum-voxel compounding. Image and tracking data were recorded through PLUS and triggered via the PLUS remote for 3DSlicer.

Reconstructed volumes were analysed using a Python pipeline with the 3DSlicer application programming interface (API). Intensity thresholding and connected-component analysis separated the four geometric targets, after which geometric descriptors were calculated, including the volume, surface area, centroid location, Feret diameter, roundness, flatness, elongation, and principal axes of variation [35].

Reference models derived from physical measurements of the agar objects were reconstructed in 3DSlicer VTK and co-registered with the corresponding segmented shapes using Iterative Closest Point (ICP) registration. For quantitative evaluation, 3DSlicer’s Segment Comparison and Segment Statistics modules were used. Agreement between predicted (X) and reference (Y) geometries was measured using the Dice

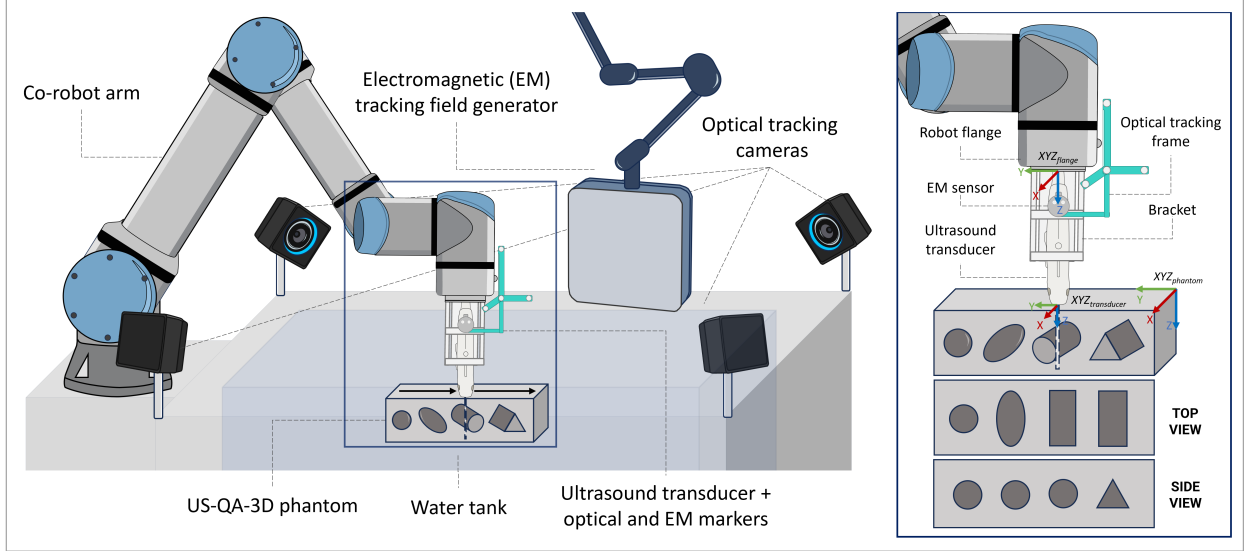


Figure 2: Experimental setup for experiments with US-QA-3D phantom, showing the robotic arm, ultrasound transducer, tracking assembly, water tank with geometric phantom, optical cameras, and electromagnetic field generator. The co-robotic arm was used for navigation. An EM sensor and an optical tracking frame enable simultaneous multimodal tracking alongside the robot’s kinematics. The reference frames for the robot flange (XYZ_{flange}), transducer ($XYZ_{transducer}$), and phantom ($XYZ_{phantom}$) are shown. The US-QA-3D phantom with geometric inclusions is shown in oblique, top, and side views.

Similarity Coefficient (DSC):

$$DSC = \frac{2|X \cap Y|}{|X| + |Y|} \quad (1)$$

In 2D, DSC measured the pixel-wise agreement between predicted and manually annotated segmentation masks, whereas in 3D (DSC-3D), it quantified voxel-wise agreement between reconstructed and reference volumes.

Boundary accuracy was assessed using the Hausdorff Distance (HD), which measures the difference between the surfaces of the predicted shape (X_s) and reference shape (Y_s). For each surface point ($x \in X_s$) and ($y \in Y_s$), the set of shortest distances to the corresponding shape ($d_{X_s \rightarrow Y_s}$ and $d_{Y_s \rightarrow X_s}$) was calculated:

$$d_{X_s \rightarrow Y_s} = \left\{ \min_{y \in Y_s} \|x - y\| : x \in X_s \right\} \quad (2)$$

$$d_{Y_s \rightarrow X_s} = \left\{ \min_{x \in X_s} \|y - x\| : y \in Y_s \right\} \quad (3)$$

This was used to find the (bidirectional) maximum Hausdorff Distance (HD_{max}), defined by the maximum of both sets of shortest distances:

$$HD(X_s, Y_s) = \max(\max(d_{X_s \rightarrow Y_s}), \max(d_{Y_s \rightarrow X_s})) \quad (4)$$

and the 95th-percentile HD (HD_{95}):

$$HD_{95}(X, Y) = \max(P_{95}(d_{X \rightarrow Y}), P_{95}(d_{Y \rightarrow X})) \quad (5)$$

Both the HD and 95th Percentile Hausdorff Distance (HD95) are positive values expressed in millimetres, with 0 mm indicating a perfect prediction.

To complement voxel-based metrics, shape-fitting provided geometry-specific information. Surface meshes

were converted to point clouds and fitted using SciPy optimisation to estimate the sphere centre and radius; ellipsoid centre and three semi-axes; cylinder centre, radius, height, and axis; and triangular prism height, axis orientation, and base vertices.

3 Results

3.1 System Performance

Our system for tracked US reconstruction demonstrated reliable, real-time performance in multimodal tracking QA experiments (Table 1). Tight synchronisation and low system latency were essential for accurate real-time 3D reconstruction and visualisation. Frame-by-frame synchronisation was handled using PLUS’s internal buffering, with a local time offset uncertainty of < 0.5 ms, as measured by the FCal temporal calibration algorithm. End-to-end latency from US capture to visualisation was approximately 90.2 ± 7.4 ms, consistent with expected delays for image transfer and display using PLUS/OpenIGTLink and 3DSlicer [21]. Volume reconstruction and VTK rendering allowed live updates every 0.2s.

Accurate tracking and registration were also critical to achieve sub-millimetre precision in the output volumes. Image-to-transducer calibration with the N-wire technique gave a Root mean square (RMS) error of 0.81 ± 0.15 mm, consistent with the reported performance of this technique [33]. Robotic kinematic tracking using the robot arm’s internal joint transformations yielded highly accurate end-effector tracking, with reported pose positioning errors of < 0.03 mm. Optical tracking calibration achieved a mean reprojection 3D error of < 0.1 mm across all experiments, but tracking was affected by marker visibility, leading to gaps in the reconstructed volumes when the line of sight was obstructed. EM tracking accuracy was limited by field distortion, despite careful placement of the EM field generator to minimise it. The RMS error was 0.1-0.2 mm in controlled conditions but increased depending on the tracker’s position relative to the robot, sometimes exceeding several millimetres. Spatial alignment across tracking modalities had a mean RMS registration error of 0.19 ± 0.07 mm.

Table 1: System performance, including timing and synchronisation, calibration and registration, and tracking accuracy.

	Metric	Value
System Timing	Synchronisation uncertainty	< 0.5 ms
	End-to-end latency	90.2 ± 7.4 ms
	Volume update rate	0.2 s
Calibration and registration	Image-to-transducer RMS error	0.81 ± 0.15 mm
	Cross-modality RMS registration error	0.19 ± 0.07 mm
Tracking Accuracy	Robot kinematic tracking accuracy	< 0.03 mm
	Optical tracking reprojection error	< 0.1 mm
	EM tracking RMS error	0.1 – 0.2 mm

3.2 Geometric phantom

Evaluation using the US-QA-3D phantom enabled controlled assessment of reconstruction accuracy, confirming the system’s ability to reconstruct known 3D shapes with low error. Combined, voxel-, surface-, shape-, and fit-based metrics provided a comprehensive evaluation of system performance under controlled conditions and highlighted the importance of accurate tracking and consistent scanning for high-quality 3D reconstruction.

Construction of the US-QA-3D phantom was straightforward, and B-mode imaging showed good contrast between the anechoic inclusions and speckle pattern of the outer media (Fig. 3a). The segmentation algorithm was tuned to define the ROI, segment the inclusions, and optimise kernels for post-processing. Small bubbles introduced to the agar inclusions during manufacturing did not affect segmentation, as closed-contour filling reliably removed them. Automatic thresholding-based segmentation delineated the inclusions accurately (Fig. 3b). Comparison with hand-annotated ground truth images (Fig. 3c) showed excellent

agreement, with a mean DSC of 0.97 on a test dataset of 50 images. The thresholding approach was also computationally efficient, with a processing time of 21.8 ± 6.4 ms on a mid-range processor.

The segmentation model was applied for real-time 3D-tracked US reconstruction with robotic navigation and simultaneous optical, EM, and kinematic tracking. During scanning, reconstructed volumes were rendered and updated in real time (Supplementary Video), allowing the operator to confirm complete coverage of the ROI (Fig. 4a). A second 3D view displayed the robot, transducer, and tracked US frames (Fig. 4b). The live US machine feed and B-mode images were shown in a dedicated 2D view (Fig. 4c), while a second 2D view displayed the segmentation overlay (Fig. 4d).

Baseline reconstruction quality was evaluated using segmentation-, shape-, and fitting-based metrics, averaged across the four geometric targets (Table 2). Robotic kinematic and optical tracking performed well, with mean DSC-3D of 0.94 ± 0.01 and 0.93 ± 0.01 , respectively, while EM-based reconstruction was poorer, with DSC-3D of 0.86 ± 0.02 , likely due to the influence of EMI. This is also supported by the HD and HD95, which measure the surface fidelity of the reconstructed shapes. For robotic kinematic and optical tracking, the maximum HD was < 2 mm and HD95 remained < 1.2 mm, but EM-tracked reconstruction had a HD95 > 2 mm. Fig. 5a shows segmented surfaces from the same imaging sequence using each tracking method, coloured by surface error relative to the co-registered ground truth.

Table 2: Baseline scans of the US-QA-3D phantom, using simultaneous tracking with robotic kinematic, optical and electromagnetic (EM) tracking. Fitting metrics provide the following shape measurements: sphere radius (R); ellipsoid semi-major axis (R1) and semi-minor axis (R2) radii; cylinder radius (R) and height (H); and triangular prism length (L) and height (H). All metrics are given as mean \pm standard deviation. The error relative to the ground truth is shown in brackets for the fitting metrics.

		Robotic	Optical	EM
Segmentation metrics	DSC-3D	0.94 ± 0.01	0.93 ± 0.01	0.86 ± 0.02
	HD (mm)	1.79 ± 0.37	1.93 ± 0.73	3.87 ± 0.87
	HD95 (mm)	1.17 ± 0.12	1.19 ± 0.12	2.43 ± 0.44
Shape metrics	Volume error (%)	11.80 ± 1.73	11.90 ± 1.47	20.05 ± 4.77
	Surface Area error (%)	8.90 ± 2.33	10.41 ± 6.76	18.10 ± 8.54
	Sphere roundness	0.98 ± 0.01	0.98 ± 0.01	0.95 ± 0.01
	Ellipsoid elongation	2.08 ± 0.01	2.07 ± 0.04	1.80 ± 0.02
Fitting metrics	Sphere R (mm)	$12.05 \pm 0.03 (+0.48)$	$12.07 \pm 0.01 (+0.50)$	$12.13 \pm 0.09 (+0.56)$
	Ellipsoid R1 (mm)	$12.73 \pm 0.09 (+0.40)$	$12.83 \pm 0.37 (+0.50)$	$14.75 \pm 0.11 (+2.42)$
	Ellipsoid R2 (mm)	$26.56 \pm 0.11 (+1.91)$	$26.59 \pm 0.07 (+1.94)$	$26.74 \pm 0.13 (+2.09)$
	Cylinder R (mm)	$11.23 \pm 0.08 (-0.73)$	$11.14 \pm 0.08 (-0.82)$	$11.93 \pm 0.26 (-0.03)$
	Cylinder H (mm)	$44.94 \pm 0.40 (+2.37)$	$45.14 \pm 0.13 (+2.57)$	$45.00 \pm 0.46 (+2.43)$
	Triangular prism L (mm)	$22.33 \pm 0.47 (-1.18)$	$22.42 \pm 0.26 (-1.09)$	$24.87 \pm 0.96 (+1.36)$
	Triangular prism H (mm)	$38.54 \pm 0.07 (+1.56)$	$38.71 \pm 0.35 (+1.73)$	$40.69 \pm 0.85 (+3.71)$

Shape-based metrics provided additional validation on the geometric reconstruction accuracy. The roundness of the segmented sphere was 0.98 ± 0.01 for both robotic and optical tracking, close to the expected value of 1.0. The ellipsoid elongation was 2.07 ± 0.01 for robotic tracking and 2.06 ± 0.01 for optical tracking, both close to the expected value of 2.0. EM-tracked reconstructions were visually poorer, with a sphere roundness of 0.95 ± 0.01 and ellipsoid elongation of 1.80 ± 0.02 indicating shape distortion.

Fit-based shape analysis also demonstrated low parameter errors for sphere and ellipsoid models under robotic and optical tracking. Fitted radii deviated by less than 0.5 mm for the sphere Radius R , and for the ellipsoid semi-axis radii R_y and R_z , but were slightly higher for R_x , potentially due to variation in lateral image resolution across the wide virtual convex imaging window. The cylinder and triangular prism also exhibited slightly higher parameter errors for dimensions along the lateral axis (x-axis), with fitted dimensions up to 2.57 mm larger than the measured values (for the cylinder reconstructed with optical tracking). Despite this, all shape-fitting functions converged successfully with low residual error.

The largest errors were observed when segmentation quality was poor, particularly in cases of surface dropout, which was occasionally seen with EM tracking. Depending on the scan orientation, shapes were also slightly elongated in the elevational direction, resulting in errors up to 1 mm in the fitted shape parameters.

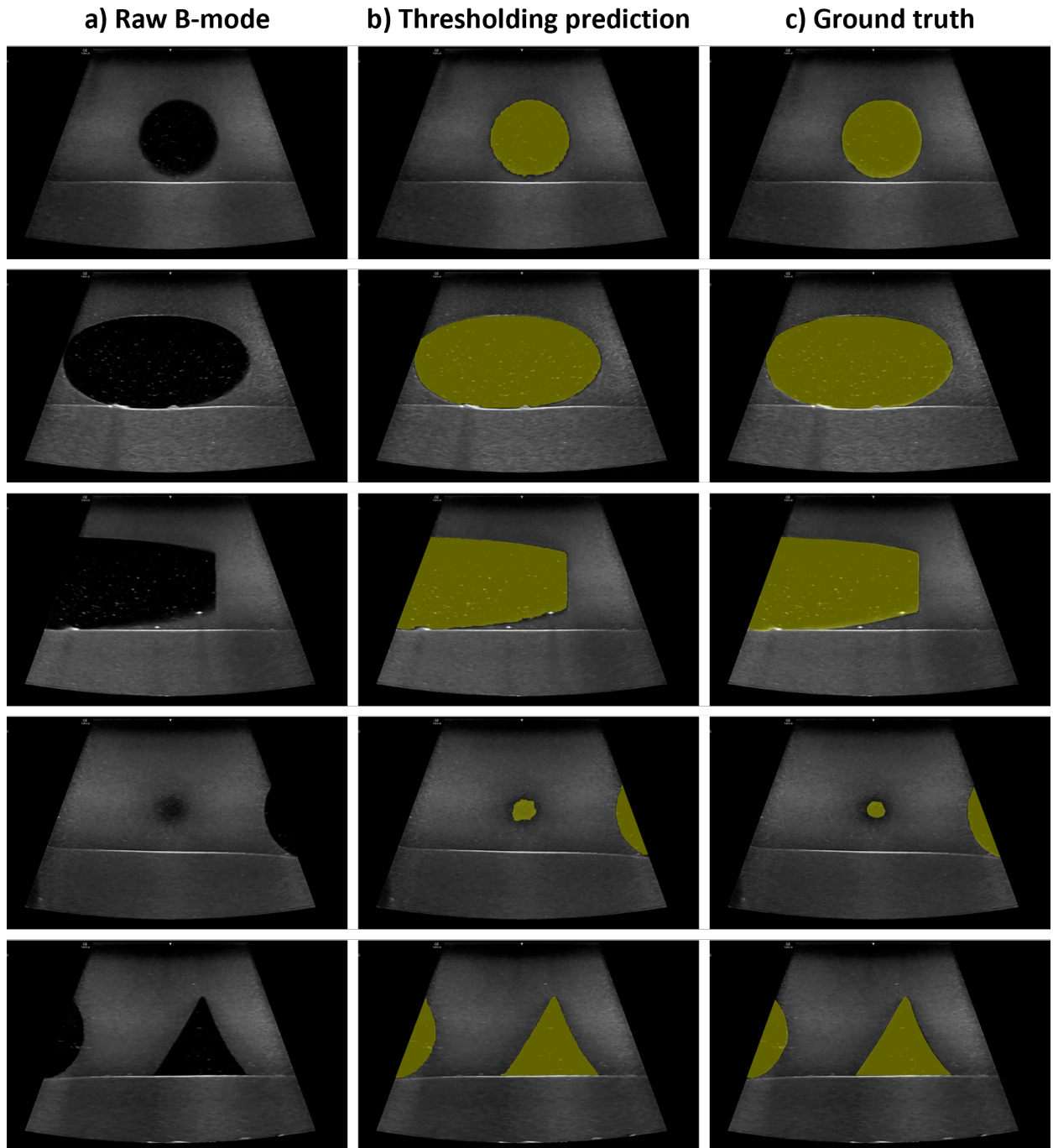


Figure 3: Thresholding-based segmentation of objects in the US-QA-3D phantom. Comparison shows a) B-mode images, b) B-mode images with overlaid prediction mask, and c) B-mode images with overlaid ground-truth reference mask.

This was likely due to the transducer's elevation thickness (0.7-2.0 mm), which causes signal spill-out from and out-of-plane elongation due to contributions above or below the imaging plane. In most cases, the shape-fitting parameters slightly exceeded the reference values, indicating a small bias toward overestimating the size of the reference objects.

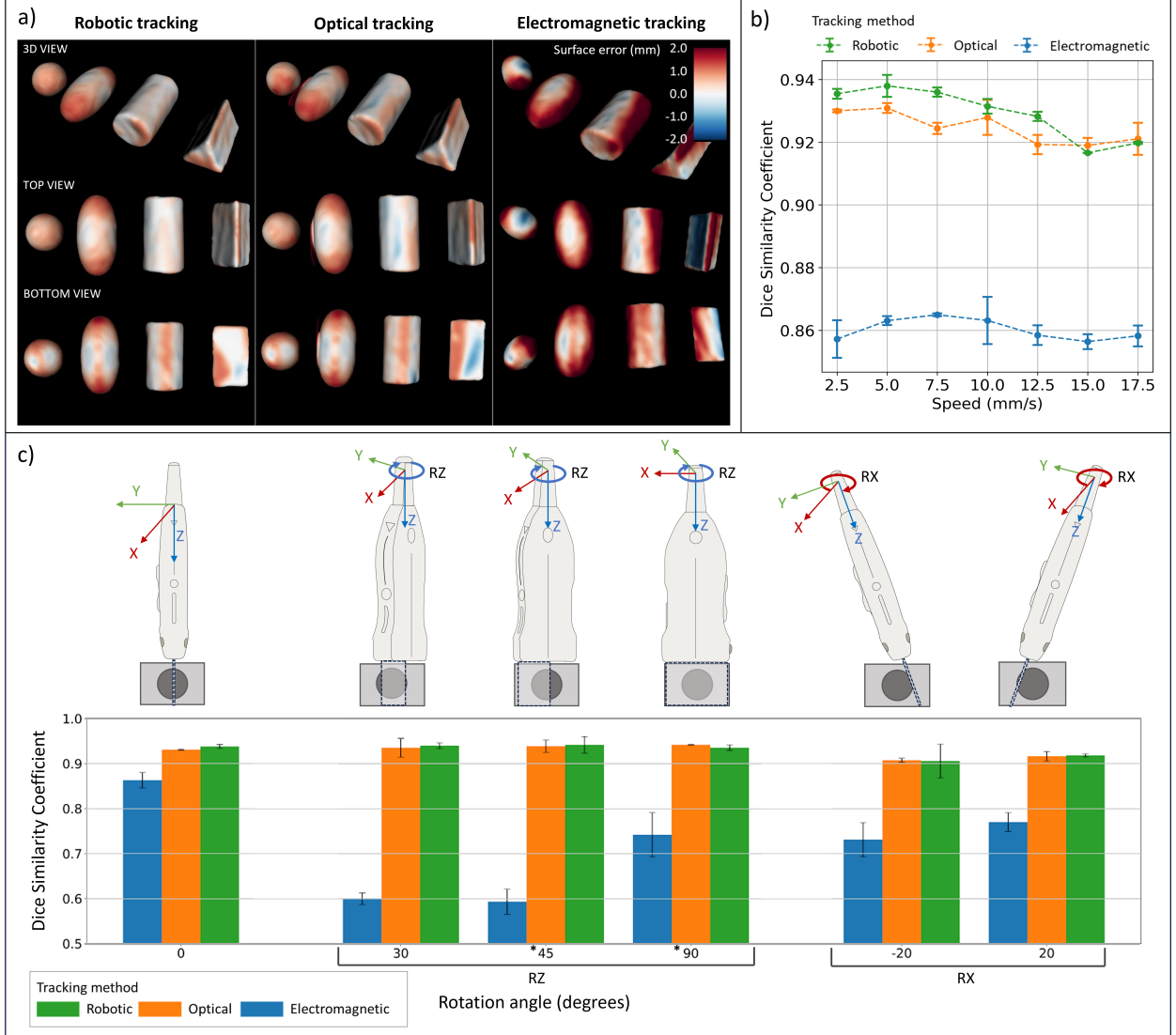


Figure 5: 3D reconstruction of objects in US-QA-3D phantom for different tracking modalities (robotic, optical, and electromagnetic). a) Heat maps show the surface deviation error compared with co-registered reference objects. b) Mean DSC across shapes at different scanning speeds. c) Mean DSC at varying insonation angles. Error bars show the standard deviation across three repeats. *These experiments required multi-sweep (compound) scanning.

Comparison with resolution-limited theoretical maximums indicated that reconstruction accuracy was largely constrained by US imaging rather than calibration, tracking, synchronisation, or segmentation. For example, given a reference sphere of radius r , the volume V is

$$V = 4/3 \cdot \pi r^3, \quad (6)$$

and a reconstructed sphere with radius error r' , the volume V' is

$$V' = 4/3 \cdot \pi (r + r')^3. \quad (7)$$

If the spheres are perfectly aligned and concentric, the theoretical resolution-limited DSC-3D is

$$\frac{2V}{V + V'} = \frac{2r^3}{r^3 + (r + r')^3} \quad (8)$$

In the US-QA-3D phantom, the sphere had radius $r = 11.5$ mm and a resolution-limited uncertainty $r' = 0.5$ mm, which gives an expected maximum DSC-3D of 0.94, closely matching the experimental values of 0.94 ± 0.01 for robotic, and 0.93 ± 0.01 for optical-tracked 3D reconstruction. Similarly, the theoretical resolution-limited sphere volume error is approximately 12%, close to the experimental values of 11.80 ± 1.73 and 11.90 ± 1.47 .

Best results were obtained using slow, constant scanning speeds, with slight degradation in reconstruction quality when the scanning speed exceeded 7.5 mm/s (Fig. 5b). At speeds ≤ 7.5 mm/s, robotic tracking performed as well as or slightly better than optical tracking and was much better than EM tracking. Under these conditions, reconstruction was both accurate and repeatable, with a mean DSC-3D > 0.92 and HD95 < 1.2 mm. At higher navigation speeds, reconstruction quality remained acceptable but decreased slightly for both robotic and optical tracking, likely due to minor synchronisation errors producing surface unevenness and small gaps. Overall, robotic tracking produced the most consistent reconstructions, followed closely by optical tracking, while EM tracking performed worse when used alongside the robot arm.

For robotic and optical tracking, insonation angle had little or no effect on the mean DSC-3D, even during multi-sweep scanning (Fig. 5c). Axial rotations (z-axis) produced accurate reconstructions despite the non-zero angle between the normal vector of the imaging plane and the scanning direction. For rotations $> 30^\circ$, maximum-value compounding enabled complete reconstruction, with no clear demarcation between the sections from multi-sweep scanning. Rotations about the lateral axis (x-axis) introduced an oblique angle between the transducer face and the phantom surface, increasing artefacts from reflection and refraction and slightly reducing the DSC-3D compared with perpendicular scanning. Across all experiments, the standard deviation between repeats was small, demonstrating good repeatability. In EM scanning experiments, the DSC-3D of the reconstructed shape was more angle-dependent since field distortion effects varied with the relative angle between the sensor and the scanner, as well as the robot position.

4 Discussion and Conclusion

This study presents a flexible, open source tracked US platform for 3D reconstruction and a standardised QA framework for quantitative system validation. We demonstrate that accurate volumetric reconstruction can be achieved with a conventional 2D B-mode transducer combined with interchangeable pose tracking using robotic kinematic, optical, or EM tracking. The platform also supports simultaneous multimodal tracking, which enables co-registered applications with other tracked tools or external systems.

Compared with existing phantom-based validation approaches designed for dedicated 3D transducers, the US-QA-3D framework evaluates volumetric shape reconstruction to expose clinically relevant failure modes of tracked US, including shape distortion, boundary noise, and scaling errors [37]. The US-QA-3D phantom incorporates shapes with different symmetry properties, helping to identify errors from calibration, temporal misalignment of data streams, anisotropic distortion in tracking, and reconstruction artefacts that may not be visible in point-based tests. The phantom was inexpensive and simple to construct, and the geometry of the inclusions could be adapted to different applications. Using threshold-based segmentation and automatic registration enabled simple QA without GPUs or specialised hardware, further simplifying implementation. Segmentation of B-mode images achieved high accuracy (DSC = 0.97) and real-time performance (45 FPS), demonstrating its suitability for assessing errors associated with tracking and 3D reconstruction. This effectively decouples tracking and reconstruction errors from segmentation errors, a distinction often overlooked in prior studies. By separating these components, the QA framework enables

meaningful comparisons for different systems, transducers, and tracking modalities and provides a practical tool to accelerate future development.

Applying this framework showed that both robotic kinematic tracking and optical tracking can achieve shape reconstruction close to the physics-based resolution limits of the US transducer ($DSC-3D = 0.94$, $HD95 = 1.2$ mm). This is significant because optical tracking is highly accurate, with widely reported sub-millimetre RMS positional accuracy [38]. Demonstrating performance comparable to optical tracking confirms that modern 6-DOF robots can provide sufficiently accurate pose tracking for high-quality 3D US, while eliminating the line-of-sight issues and workflow complexity associated with optical cameras. The QA also clarified the role of EM tracking in tracked US, which performed well in freehand calibration, but poorly when used alongside the robot arm. This is consistent with the well-documented susceptibility of EM tracking to magnetic field distortion [39] and highlights the importance of volumetric QA when using EM tracking in clinical settings, where ferromagnetic objects and EMI sources are often unavoidable [39].

Nevertheless, there are important limitations in this study that should form the basis for future research. This study used a single high-frequency linear probe, and further investigation is needed to evaluate performance with other transducers, systems, and imaging settings. Furthermore, while the QA framework assessed geometric reconstruction under controlled conditions, future work should investigate robustness in non-idealised settings to quantify the additional effect of tissue deformation, acoustic shadowing, and patient motion on 3D reconstruction. Finally, although optical, EM, and robotic kinematic tracking have been the dominant techniques for US tracking, recent trackerless methods have also been developed that use AI models to estimate transducer trajectories from video clips [12, 40, 41, 42]. These methods, while promising, were not assessed here as they remain difficult to validate quantitatively and are not yet suitable for safety-critical image-guided interventions.

By standardising volumetric QA for tracked US, this work supports transparent performance reporting and facilitates cross-system comparison and evidence-based development of 3D US. The proposed system showed accurate 3D reconstruction with robotic, optical, and EM tracking which makes it extensible to a range of previously investigated clinical applications, including 3D reconstruction for organ volumetry [43], vascular assessment to determine the severity of stenosis [44, 14, 45], and HIFU treatment planning for tumour ablation [46]. Ultimately, the framework will improve confidence in the reliability of 3D US reconstruction, which is essential for safe and effective translation in clinical practice.

5 Acknowledgments

This study has received funding from the Engineering and Physical Sciences Research Council (EPSRC) through the following awards: EP/S024336/1 and EP/V04799X/1. J. Chandler was supported by the Leverhulme Trust and the Royal Academy of Engineering under a RAEng/Leverhulme Trust Research Fellowship (LTRF-2425-21-154).

6 Appendix

6.1 US-QA-3D phantom fabrication

Silicone moulds of reference objects were created by casting negative impressions of wooden masters. Moulds were made of platinum-cure silicone (Smooth-On, Dragon Skin 10 Medium) in 3D-printed moulds with pour and vent channels (Fig. 6a). These were then filled with an agar mixture with no acoustic scatterers to form solid inclusions which appear anechoic on B-mode US. These objects were removed from the moulds, the sprues trimmed, and the objects were measured to obtain ground-truth dimensions (Fig. 6b). Four reference objects were created with varying geometric and symmetry properties: a sphere (Fig. 6c), an ellipsoid (spheroid) (Fig. 6d), a right circular cylinder (Fig. 6e), and an equilateral triangular prism (Fig. 6f). The

inclusions were then set in a larger agar block, this time adding glass beads to introduce speckle noise in B-mode images (mimicking heterogeneous tissue), thereby creating contrast with the anechoic inclusions. A flat layer approximately 3 cm deep (one-third of the agar) was poured, allowed to cool, and mostly solidify, while the remainder was kept warm. The anechoic inclusions were then placed on top of the first layer, and a second layer was poured to surround and cover the inclusions (remaining two-thirds). Once fully set, the phantom was vacuum-sealed for longevity, and the appearance of inclusions was confirmed on B-mode. The recipe for making the agar mixtures is below and can be scaled to the required volume. STL files for 3D-printed parts are available at <https://github.com/SMRTUS/US-QA-3D>.

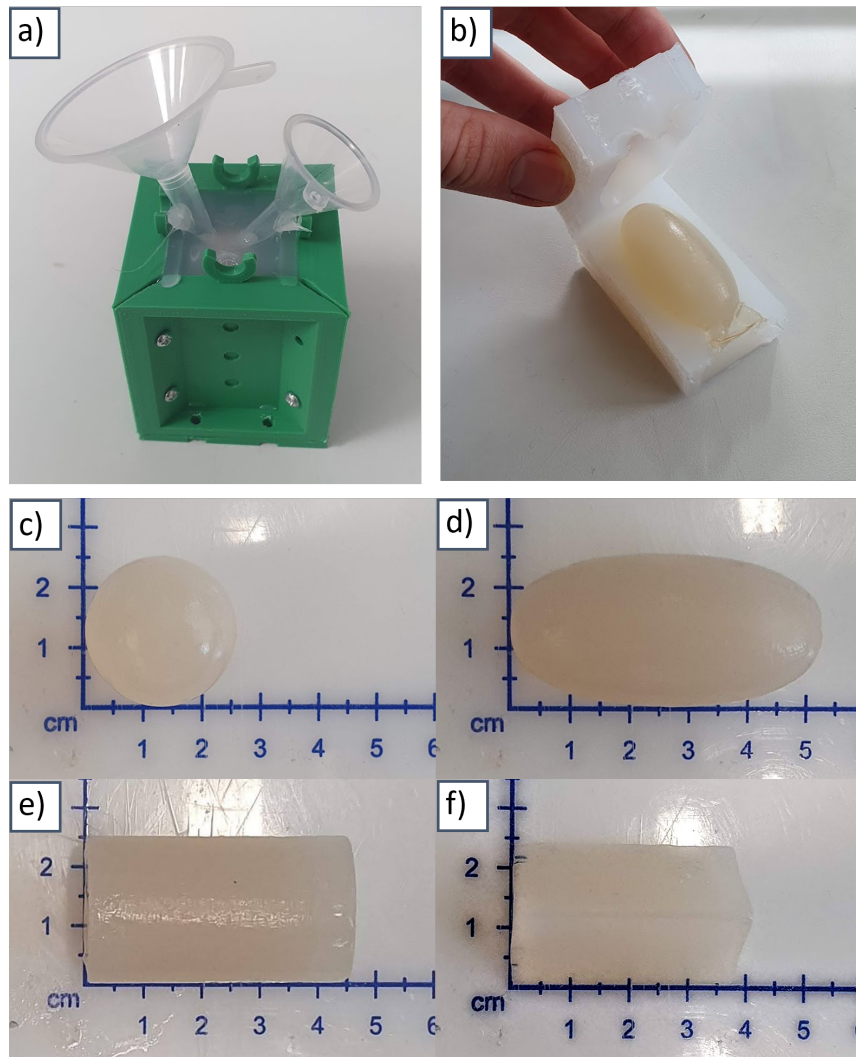


Figure 6: US-QA-3D phantom construction showing a) fabrication of silicone mould of reference object in 3D-printed container, b) silicone mould with agar inclusion (before trimming the sprue), c-f) agar sphere, ellipsoid, cylinder, and triangular prism reference objects.

For ~250ml of agar:

- 250 mL deionised water,
- 12.5 g agar-agar,
- 25 mL glycerol $\geq 99\%$ (increases speed of sound),
- 2.5 mL phenoxyethanol EHG (preservative),
- *10 g glass beads (soda lime glass microspheres, 3-6 μm diameter, introduces heterogeneity/speckle).

1. Transfer deionised water into a Büchner flask and heat to 70–75 °C.
2. Slowly add agar-agar, stirring continuously to prevent clumping. Add the glycerol. *Optionally add the glass beads for a tissue-mimicking material, exclude for anechoic material.
3. Apply a vacuum and degass the mixture for 20–30 min.
4. Slowly release the vacuum, then carefully pour into the mould(s). Allow to cool and set at room temperature.

References

- [1] Z. Chenhao, Z. Ruqi, S. Xiaozhuo, W. Jiabo, L. Jiao, and M. Yajuan, “Ultrasound in medicine from 2014 to 2024: A bibliometric review,” *Medicine*, vol. 105, no. 2, p. e46890, Jan. 2026. [Online]. Available: <https://pmc.ncbi.nlm.nih.gov/articles/PMC12795102/>
- [2] N. M. Bekedam, J. N. Smit, P. K. de Koekoek Doll, M. J. A. van Alphen, R. L. P. van Veen, L. H. E. Karssemakers, M. B. Karakullukcu, and L. E. Smeele, “Intra-operative resection margin model of tongue carcinoma using 3D reconstructed ultrasound,” *Advances in Oral and Maxillofacial Surgery*, vol. 4, p. 100154, Oct. 2021. [Online]. Available: <https://www.sciencedirect.com/science/article/pii/S2667147621001436>
- [3] P. Chatelain, A. Krupa, and N. Navab, “3D ultrasound-guided robotic steering of a flexible needle via visual servoing,” in *2015 IEEE International Conference on Robotics and Automation (ICRA)*, May 2015, pp. 2250–2255. [Online]. Available: <https://ieeexplore.ieee.org/document/7139497>
- [4] D. Li, Z. Cheng, G. Chen, F. Liu, W. Wu, J. Yu, Y. Gu, F. Liu, C. Ren, and P. Liang, “A multimodality imaging-compatible insertion robot with a respiratory motion calibration module designed for ablation of liver tumors: a preclinical study,” *International Journal of Hyperthermia*, vol. 34, no. 8, pp. 1194–1201, Nov. 2018. [Online]. Available: <https://doi.org/10.1080/02656736.2018.1456680>
- [5] T. Boers, S. J. Braak, W. M. Brink, M. Versluis, and S. Manohar, “3D ultrasound guidance for radiofrequency ablation in an anthropomorphic thyroid nodule phantom,” *European Radiology Experimental*, vol. 8, no. 1, p. 115, Oct. 2024. [Online]. Available: <https://doi.org/10.1186/s41747-024-00513-6>
- [6] L. J. Howell, V. W.-S. Chan, J. Zhong, H. H.-L. Ng, J. H. Chandler, J. R. McLaughlan, and T. M. Wah, “Histotripsy: New Frontiers for Noninvasive Ablation,” *The Arab Journal of Interventional Radiology*, vol. 9, no. 2, p. 61, Dec. 2025. [Online]. Available: https://journals.lww.com/ajir/fulltext/2025/07000/histotripsy__new_frontiers_for_noninvasive.1.aspx
- [7] C. Y. An, J. H. Syu, C. S. Tseng, and C.-J. Chang, “An Ultrasound Imaging-Guided Robotic HIFU Ablation Experimental System and Accuracy Evaluations,” *Applied Bionics and Biomechanics*, vol. 2017, p. e5868695, Apr. 2017. [Online]. Available: <https://www.hindawi.com/journals/abb/2017/5868695/>
- [8] H. H. L. Ng, V. W.-S. Chan, L. Howell, T. Shiwani, J. Zhong, J. Brandon, A. Samson, J. Chandler, J. McLaughlan, and T. M. Wah, “Early Adoption of Image-Guided Histotripsy Therapy in Interventional Oncology: Challenges and Opportunities in the UK,” *British Journal of Radiology*, p. tqag047, Mar. 2026. [Online]. Available: <https://doi.org/10.1093/bjr/tqag047>
- [9] Q. Huang and Z. Zeng, “A Review on Real-Time 3D Ultrasound Imaging Technology,” *BioMed Research International*, vol. 2017, p. 6027029, 2017.

-
- [10] Y. Wang, Q. Yang, L. Drukker, A. Papageorghiou, Y. Hu, and J. A. Noble, "Task model-specific operator skill assessment in routine fetal ultrasound scanning," *International Journal of Computer Assisted Radiology and Surgery*, vol. 17, no. 8, pp. 1437–1444, 2022. [Online]. Available: <https://pmc.ncbi.nlm.nih.gov/articles/PMC9307537/>
- [11] F. Mohamed, C. V. Siang, F. Mohamed, and C. V. Siang, "A Survey on 3D Ultrasound Reconstruction Techniques," in *Artificial Intelligence - Applications in Medicine and Biology*. IntechOpen, Apr. 2019. [Online]. Available: <https://www.intechopen.com/chapters/63949>
- [12] C. Peng, Q. Cai, M. Chen, and X. Jiang, "Recent Advances in Tracking Devices for Biomedical Ultrasound Imaging Applications," *Micromachines*, vol. 13, no. 11, p. 1855, Oct. 2022. [Online]. Available: <https://pmc.ncbi.nlm.nih.gov/articles/PMC9695235/>
- [13] M. H. Mozaffari and W.-S. Lee, "Freehand 3-D Ultrasound Imaging: A Systematic Review," *Ultrasound in Medicine & Biology*, vol. 43, no. 10, pp. 2099–2124, Oct. 2017.
- [14] S.-W. Chung, C.-C. Shih, and C.-C. Huang, "Freehand three-dimensional ultrasound imaging of carotid artery using motion tracking technology," *Ultrasonics*, vol. 74, pp. 11–20, Feb. 2017. [Online]. Available: <https://www.sciencedirect.com/science/article/pii/S0041624X16302001>
- [15] M. Krönke, C. Eilers, D. Dimova, M. Köhler, G. Buschner, L. Schweiger, L. Konstantinidou, M. Makowski, J. Nagarajah, N. Navab, W. Weber, and T. Wendler, "Tracked 3D ultrasound and deep neural network-based thyroid segmentation reduce interobserver variability in thyroid volumetry," *PLOS ONE*, vol. 17, no. 7, p. e0268550, Jul. 2022. [Online]. Available: <https://journals.plos.org/plosone/article?id=10.1371/journal.pone.0268550>
- [16] A. M. Priester, S. Natarajan, and M. O. Culjat, "Robotic ultrasound systems in medicine," *IEEE Transactions on Ultrasonics, Ferroelectrics, and Frequency Control*, vol. 60, no. 3, pp. 507–523, Mar. 2013. [Online]. Available: <https://ieeexplore.ieee.org/document/6470412>
- [17] G. Faoro, S. Maglio, S. Pane, V. Iacovacci, and A. Menciassi, "An Artificial Intelligence-Aided Robotic Platform for Ultrasound-Guided Transcarotid Revascularization," *IEEE Robotics and Automation Letters*, vol. 8, no. 4, pp. 2349–2356, Apr. 2023. [Online]. Available: <https://ieeexplore.ieee.org/document/10057986>
- [18] D. Sun, A. Cappellari, B. Lan, M. Abayazid, S. Stramigioli, and K. Niu, "Automatic Robotic Ultrasound for 3D Musculoskeletal Reconstruction: A Comprehensive Framework," *Technologies*, vol. 13, no. 2, p. 70, Feb. 2025. [Online]. Available: <https://www.mdpi.com/2227-7080/13/2/70>
- [19] A. Schmidt, O. Mohareri, S. DiMaio, M. C. Yip, and S. E. Salcudean, "Tracking and mapping in medical computer vision: A review," *Medical Image Analysis*, vol. 94, p. 103131, May 2024.
- [20] J. Tokuda, G. S. Fischer, X. Papademetris, Z. Yaniv, L. Ibanez, P. Cheng, H. Liu, J. Blevins, J. Arata, A. J. Golby, T. Kapur, S. Pieper, E. C. Burdette, G. Fichtinger, C. M. Tempany, and N. Hata, "OpenIGTLink: an open network protocol for image-guided therapy environment," *The international journal of medical robotics and computer assisted surgery*, vol. 5, no. 4, pp. 423–434, Dec. 2009. [Online]. Available: <https://www.ncbi.nlm.nih.gov/pmc/articles/PMC2811069/>
- [21] A. Lasso, T. Heffter, A. Rankin, C. Pinter, T. Ungi, and G. Fichtinger, "PLUS: Open-source toolkit for ultrasound-guided intervention systems," *IEEE Transactions on Biomedical Engineering*, vol. 61, pp. 2527–2537, 2014.

-
- [22] T. Ungi, A. Lasso, and G. Fichtinger, “Open-source platforms for navigated image-guided interventions,” *Medical Image Analysis*, vol. 33, pp. 181–186, Oct. 2016. [Online]. Available: <https://www.sciencedirect.com/science/article/pii/S1361841516300895>
- [23] Computerized Imaging Reference Systems Inc., “Multi-Purpose, Multi-Tissue Ultrasound Phantom,” 2013.
- [24] Universal Robots, “Universal Robot PolyScope X 10.11.1 UR3e,” 2025. [Online]. Available: https://www.universal-robots.com/manuals/EN/HTML/SW10_11/Content/Landingpages/WebPolyX/LandingPDFX.htm
- [25] L. Connolly, A. Deguet, S. Leonard, J. Tokuda, T. Ungi, A. Krieger, P. Kazanzides, P. Mousavi, G. Fichtinger, and R. H. Taylor, “Bridging 3D Slicer and ROS2 for Image-Guided Robotic Interventions,” *Sensors (Basel, Switzerland)*, vol. 22, no. 14, p. 5336, Jul. 2022. [Online]. Available: <https://www.ncbi.nlm.nih.gov/pmc/articles/PMC9324680/>
- [26] “moveit/moveit2,” Oct. 2025. [Online]. Available: <https://github.com/moveit/moveit2>
- [27] OptiTrack (NaturalPoint Inc.), “Calibration v2.3 OptiTrack Documentation,” Oct. 2022. [Online]. Available: <https://docs.optitrack.com/v2.3/motive/calibration>
- [28] A. Sun, “alvinsunyixiao/vrpn_mocap,” Sep. 2025. [Online]. Available: https://github.com/alvinsunyixiao/vrpn_mocap
- [29] Tobias Frank and Junichi Tokuda, “openigtlink/ros2_igt1_bridge,” Dec. 2024. [Online]. Available: https://github.com/openigtlink/ros2_igt1_bridge
- [30] Northern Digital Inc, “Minimally Invasive Procedures with Electromagnetic Tracking Technology,” 2024. [Online]. Available: <https://www.ndigital.com/electromagnetic-tracking-technology/aurora/>
- [31] Perk Lab, “PlusLib: NDI Vega, Polaris and Aurora pose trackers,” Aug. 2025. [Online]. Available: <http://perk-software.cs.queensu.ca/plus/doc/nightly/dev/DeviceNDI.html>
- [32] Universal Robots, “DH Parameters for calculations of kinematics and dynamics,” Nov. 2026. [Online]. Available: <https://www.universal-robots.com/articles/ur/application-installation/dh-parameters-for-calculations-of-kinematics-and-dynamics/>
- [33] G. Carbajal, A. Lasso, A. Gomez, and G. Fichtinger, “Improving N-wire phantom-based freehand ultrasound calibration,” *International journal of computer assisted radiology and surgery*, vol. 8, Jul. 2013.
- [34] N. Otsu, “A Threshold Selection Method from Gray-Level Histograms,” *IEEE Transactions on Systems, Man, and Cybernetics*, vol. 9, no. 1, pp. 62–66, Jan. 1979. [Online]. Available: <https://ieeexplore.ieee.org/document/4310076/>
- [35] J. C. Russ and F. B. Neal, *The Image Processing Handbook*, 7th ed. Boca Raton: CRC Press, Sep. 2018.
- [36] M. Bozorgi and F. Lindseth, “GPU-based multi-volume ray casting within VTK for medical applications,” *International Journal of Computer Assisted Radiology and Surgery*, vol. 10, no. 3, pp. 293–300, Mar. 2015.
- [37] D. Iommi, J. Hummel, and M. L. Figl, “Evaluation of 3D ultrasound for image guidance,” *PLoS ONE*, vol. 15, no. 3, p. e0229441, Mar. 2020. [Online]. Available: <https://pmc.ncbi.nlm.nih.gov/articles/PMC7098612/>

-
- [38] A. M. Aurand, J. S. Dufour, and W. S. Marras, “Accuracy map of an optical motion capture system with 42 or 21 cameras in a large measurement volume,” *Journal of Biomechanics*, vol. 58, pp. 237–240, Jun. 2017. [Online]. Available: <https://www.sciencedirect.com/science/article/pii/S0021929017302580>
- [39] F. Poulin and L. P. Amiot, “Interference during the use of an electromagnetic tracking system under OR conditions,” *Journal of Biomechanics*, vol. 35, no. 6, pp. 733–737, Jun. 2002. [Online]. Available: <https://www.sciencedirect.com/science/article/pii/S0021929002000362>
- [40] Y. Zhou, C. Chen, J. Yao, J. Yu, B. Feng, L. Sui, Y. Yan, X. Chen, Y. Liu, X. Zhang, H. Wang, Q. Pan, W. Zou, Q. Zhang, L. Lin, C. Xu, S. Yuan, Q. He, X. Ding, P. Liang, V. Y. Wang, and D. Xu, “A deep learning based ultrasound diagnostic tool driven by 3D visualization of thyroid nodules,” *npj Digital Medicine*, vol. 8, no. 1, p. 126, Feb. 2025. [Online]. Available: <https://www.nature.com/articles/s41746-025-01455-y>
- [41] H. Yandong, Z. Shiqi, J. Lanting, H. Wenxin, C. Leyao, and H. Hejing, “Establishment and preliminary application of personalized three-dimensional reconstruction of thyroid gland with automatic detection of thyroid nodules based on ultrasound videos,” *Journal of Applied Clinical Medical Physics*, vol. 25, no. 6, p. e14332, Mar. 2024. [Online]. Available: <https://pubmed.ncbi.nlm.nih.gov/articles/PMC11163481/>
- [42] W. Wein, M. Lupetti, O. Zettinig, S. Jagoda, M. Salehi, V. Markova, D. Zonoobi, and R. Prevost, “Three-Dimensional Thyroid Assessment from Untracked 2D Ultrasound Clips,” in *Medical Image Computing and Computer Assisted Intervention – MICCAI 2020*, ser. Lecture Notes in Computer Science, A. L. Martel, P. Abolmaesumi, D. Stoyanov, D. Mateus, M. A. Zuluaga, S. K. Zhou, D. Racoceanu, and L. Joskowicz, Eds. Cham: Springer International Publishing, 2020, pp. 514–523.
- [43] J. Zielke, C. Eilers, B. Busam, W. Weber, N. Navab, and T. Wendler, “RSV: Robotic Sonography for Thyroid Volumetry,” *IEEE Robotics and Automation Letters*, vol. 7, no. 2, pp. 3342–3348, Apr. 2022. [Online]. Available: <https://ieeexplore.ieee.org/document/9695372>
- [44] S. Merouche, L. Allard, E. Montagnon, G. Soulez, P. Bigras, and G. Cloutier, “A Robotic Ultrasound Scanner for Automatic Vessel Tracking and Three-Dimensional Reconstruction of B-Mode Images,” *IEEE Transactions on Ultrasonics, Ferroelectrics, and Frequency Control*, vol. 63, no. 1, pp. 35–46, Jan. 2016. [Online]. Available: <https://ieeexplore.ieee.org/document/7322288>
- [45] K. AlMuhanna, M. M. Hossain, L. Zhao, J. Fischell, G. Kowalewski, M. Dux, S. Sikdar, and B. K. Lal, “Carotid plaque morphometric assessment with three-dimensional ultrasound imaging,” *Journal of Vascular Surgery*, vol. 61, no. 3, pp. 690–697, Mar. 2015. [Online]. Available: <https://www.sciencedirect.com/science/article/pii/S0741521414018667>
- [46] L. Daunizeau, A. Nguyen, M. Le Garrec, J. Y. Chapelon, and W. A. N’Djin, “Robot-assisted ultrasound navigation platform for 3D HIFU treatment planning: Initial evaluation for conformal interstitial ablation,” *Computers in Biology and Medicine*, vol. 124, p. 103941, Sep. 2020. [Online]. Available: <https://www.sciencedirect.com/science/article/pii/S0010482520302766>